

# GazeShift: Unsupervised Gaze Estimation and Dataset for VR

Gil Shapira<sup>1</sup> Ishay Goldin<sup>1</sup> Evgeny Artyomov<sup>1</sup>  
Donghoon Kim<sup>2</sup> Yosi Keller<sup>3</sup> Niv Zehngut<sup>1</sup>

<sup>1</sup>Samsung Semiconductor Israel R&D Center (SIRC)

<sup>2</sup>Samsung Electronics <sup>3</sup>Bar-Ilan University

{gil.shapira, ishay.goldin, evgeny.a, dhoon.kim, niv.z}@samsung.com

yosi.keller@gmail.com

## Abstract

*Gaze estimation is instrumental in modern virtual reality (VR) systems. Despite significant progress in remote-camera gaze estimation, VR gaze research remains constrained by data scarcity—particularly the lack of large-scale, accurately labeled datasets captured with the off-axis camera configurations typical of modern headsets. Gaze annotation is difficult since fixation on intended targets cannot be guaranteed. To address these challenges, we introduce VRGaze—the first large-scale off-axis gaze estimation dataset for VR—comprising 2.1 million near-eye infrared images collected from 68 participants. We further propose GazeShift, an attention-guided unsupervised framework for learning gaze representations without labeled data. Unlike prior redirection-based methods that rely on multi-view or 3D geometry, GazeShift is tailored to near-eye infrared imagery, achieving effective gaze–appearance disentanglement in a compact, real-time model. GazeShift embeddings can be optionally adapted to individual users via lightweight few-shot calibration, achieving a 1.84° mean error on VRGaze. On the remote-camera MPIIGaze dataset, the model achieves a 7.15° person-agnostic error, doing so with 10x fewer parameters and 35x fewer FLOPs than baseline methods. Deployed natively on a VR headset GPU, inference takes only 5 ms. Combined with demonstrated robustness to illumination changes, these results highlight GazeShift as a label-efficient, real-time solution for VR gaze tracking. Project code and the VRGaze dataset are released at <https://github.com/gazeshift3/gazeshift>*

## 1. Introduction

Gaze estimation is a key component in human–computer interaction [18], extended reality (XR) [26], and assistive technologies [4]. It enables hands-free interaction [28], attention-aware interfaces [19], and personalized user ex-

periences. In XR, gaze supports foveated rendering [25], intuitive input, and adaptive content delivery [6, 26], with further use in driver monitoring [17] and attention analysis [21].

Training accurate gaze estimators requires large datasets with precise labels, yet gaze cannot be directly inferred from eye images. Labels derived from predefined targets are often unreliable due to fixation uncertainty and involuntary saccades, making annotation time-consuming and error-prone [35].

Unsupervised learning, successfully applied to classification [3, 9, 10], has been recently explored for gaze estimation [30, 33] to eliminate label dependence. However, existing methods are designed for remote RGB cameras that capture full faces and have not been adapted to the distinct near-eye infrared modality of VR.

To address this gap, we introduce VRGaze, the first large-scale near-eye off-axis gaze dataset, comprising 2.1M labeled images from 68 subjects. Off-axis cameras are standard in modern VR headsets, yet no public dataset previously captured this geometry at comparable scale.

We further propose GazeShift, an unsupervised framework tailored to near-eye imaging but generalizable to remote settings. Unlike prior redirection-based methods relying on geometry [32] or complex warping fields [33], GazeShift learns gaze representations through attention-driven transformations between pairs of the same eye. In VR-mounted cameras, most appearance variation arises from gaze changes; GazeShift models this relation via cross-attention between separately encoded latent representations, enabling clean gaze–appearance disentanglement without geometric priors [30, 33].

Head-mounted cameras inherently suppress external variation, making gaze the dominant source of temporal change. GazeShift leverages this property with an attention-based reconstruction module producing spatial maps that highlight gaze-relevant regions. To suppress peripheral re-

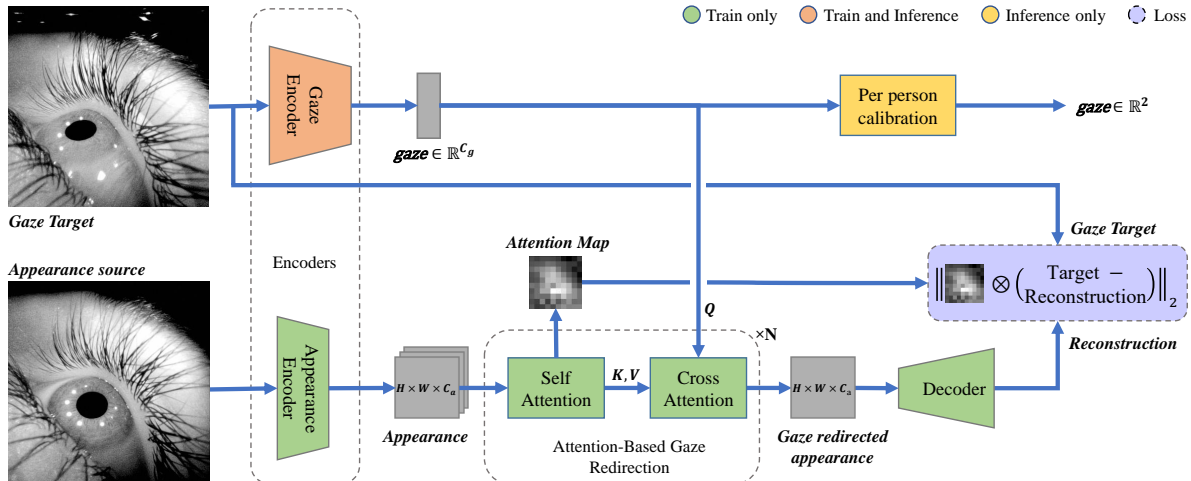


Figure 1. **GazeShift architecture.** The model is trained to reconstruct the appearance source image to match the gaze target, conditioned on the target’s gaze embedding. A lightweight gaze encoder extracts the embedding, while a separate appearance encoder preserves spatial structure. Appearance tokens undergo self-attention and cross-attention (conditioned on the gaze embedding) before being decoded. Attention maps also guide a gaze-aware loss focused on gaze-relevant regions. At inference, only the gaze encoder and a lightweight calibration module are used to predict gaze.

construction noise, we introduce a gaze-aware loss that focuses learning on regions contributing most to gaze estimation. This creates a feedback loop where refined attention improves performance, which in turn sharpens attention localization.

Evaluated on VRGaze, GazeShift achieves a mean error of  $1.84^\circ$ , nearing supervised accuracy, and generalizes to remote settings, reaching  $7.15^\circ$  on MPIIGaze with 10× fewer parameters—suitable for deployment on resource-limited headsets.

Our main contributions are:

- The first large-scale off-axis VR gaze dataset (**VRGaze**) comprising 2.1M labeled images from 68 subjects.
- An unsupervised framework that learns gaze redirection through cross-image attention and introduces a gaze-aware loss derived from internal attention, focusing learning on gaze-relevant regions without external supervision.
- Demonstrated state-of-the-art cross-modality generalization across VR and remote camera benchmarks. Underscoring its efficiency for edge deployment, the system achieves real-time 5 ms inference on a VR headset with 10x fewer parameters and 35x fewer FLOPs than the baseline.

## 2. Related Work

### 2.1. Supervised Gaze Estimation

**Near-eye cameras.** Supervised gaze estimation methods for near-eye cameras can be broadly categorized into *appearance-based*, *feature-based*, and *geometry-based* ap-

proaches. Appearance-based methods [15] employ end-to-end deep models to directly regress gaze direction from raw eye images. Feature-based methods [22] first extract cues such as the pupil center and corneal reflections (glints) before estimating gaze in a subsequent regression stage. Geometry-based methods [14, 37] instead rely on explicit eye models and calibrated setups; while highly accurate, they depend on specialized hardware and detailed knowledge of the 3D camera–illumination configuration, which is often unavailable in commercial VR/XR headsets.

**Remote cameras.** Early gaze estimation methods focused on predicting gaze direction from eye-region images alone [5, 24]. Zhang et al. [34] showed that full-face images could outperform eye-only approaches, leading subsequent research to favor face-based models [1]. As a result, most neural network–based methods in remote settings now rely on face images as their primary input—limiting their applicability to near-eye camera scenarios, where only partial facial context is available.

### 2.2. Unsupervised Gaze Estimation

Unsupervised learning reduces annotation cost by leveraging proxy tasks. Yu & Odobez [33] first introduced gaze representation learning through gaze redirection, but their model depends on complex warping fields and geometric priors. In contrast, GazeShift achieves similar redirection behavior using standard attention modules, with no task-specific components. Sun et al. [30] introduced Cross-Encoder, which jointly encodes gaze and appearance into a shared latent space. While effective, this design exposes the

Table 1. Overview of VR eye-tracking datasets.

Dataset	Year	Gaze Ann. (PoR)	Participants		Images	
			VR off-axis/Total	VR off-axis/ Total		
NVGaze [15]	2018	Yes	14/ 49	260K / 2.5M		
OpenEDS2020 [23]	2020	Yes	0/ 80	0 / 550K		
TEyeD [7]	2021	No	14/ 132	260K/ 20M		
VRGaze (ours)	2025	Yes	68/ 68	2.1M / 2.1M		

decoder to target appearance information, leading to partial leakage and limited disentanglement. In contrast, GazeShift employs two dedicated encoders—one for gaze and one for appearance—and connects them through a cross-attention mechanism. The gaze vector modulates the source appearance features via attention, effectively acting as a buffer layer that isolates the gaze encoder from the decoder and prevents appearance information from contaminating the gaze representation.

Other recent unsupervised frameworks [8, 13, 31] employ contrastive or equivariant objectives on full-face inputs, making them less applicable to headset-mounted cameras. GazeShift addresses this gap by learning directly from single-eye infrared imagery.

### 3. VRGaze Dataset

Despite the growing popularity of VR and the central role of gaze estimation within it, only a limited number of publicly available datasets address this task in VR settings. OpenEDS2020 [23] provides 550,400 gaze-labeled images from 80 participants; however, all images are captured with on-axis cameras, which do not reflect the off-axis geometry typical of commercial VR headsets (Apple Vision Pro, Meta Quest Pro, HTC VIVE Pro Eye etc.) [2, 11, 20], where cameras are mounted at oblique angles to reduce visual obstruction. This geometry introduces strong perspective distortions absent from on-axis datasets such as OpenEDS, making off-axis data essential for realistic VR gaze estimation (Figure 2). In our experiments (section 5.1), we qualitatively show that on-axis data fail to transfer well to off-axis scenarios, underscoring the importance of our off-axis VRGaze dataset.

NVGaze [15] offers a larger corpus of 2.5 million frames, yet the majority are also on-axis. Only a small subset of approximately 260K frames from 14 subjects contains off-axis views, and these lack diversity in gaze directions. TEyeD [7] is a large dataset of over 20 million eye images, but most of it was not collected in a VR environment. Additionally, it was annotated using computational methods and may not provide accurate ground truth. These differences are summarized in Table 1.

To address the scarcity of large-scale off-axis data, we introduce VRGaze, a new dataset comprising 2.1 million synchronized left and right eye images captured from 68 par-

Table 2. VRGaze dataset statistics.

Count	Gender	Ethnicity	Age (years)				Train / Val
	(F / M)	(Asian / Cauc)	18–30	31–40	41–50	51+	
14 / 54	29 / 39	22 / 30 / 13 / 3	61 / 7				

ticipants using a custom modern VR headset equipped with off-axis near-eye infrared cameras. Data were recorded at 30 fps with an image resolution of  $400 \times 400$  pixels (sample images are shown in Figure 2). The participant pool is diverse in terms of ethnicity, age, and gender (see Table 2), and all individuals provided informed consent for public release of their eye imagery.

Data were collected as participants followed a moving target on a VR display, alternating between pursuit and fixation segments. The background brightness was varied to elicit a broad range of pupil dilations.

Recordings were conducted over multiple sessions. Each participant began with a deterministic target trajectory designed to simulate calibration, followed by sessions featuring randomized target movements to emulate naturalistic viewing behavior. On average, seven sessions were recorded per participant. Seven participants were held out for validation, while the remaining were used for training. The distribution of ground-truth gaze angles – both horizontal (yaw) and vertical (pitch) – is visualized in Figure 2. Gaze labels correspond to the 2D Point of Regard (PoR) of the moving target on the VR display. These coordinates are computed from the known geometry of the headset. For validation, we consider only fixation intervals, where gaze remains stable and PoR annotations are the most reliable.

### 4. Method

We introduce GazeShift, a simple yet general attention-based framework for unsupervised gaze representation learning. Unlike prior gaze-redirection or disentanglement models that depend on geometric priors, multi-view consistency, or complex regularization schemes [16, 32, 33], GazeShift relies solely on standard attention operations to model transformations between eye images captured at different gaze directions. Its core novelty lies in a generic attention architecture free of ad hoc gaze-specific modules, and in a gaze-aware reconstruction loss that leverages the model’s own self-attention maps to automatically emphasize gaze-relevant regions. Together, these components enable effective learning of gaze-specific embeddings without labels, auxiliary detectors, or handcrafted constraints, making GazeShift both conceptually simple and broadly applicable across VR and remote-camera domains. The overall architecture is illustrated in Figure 1.

Assuming that, for a given subject and eye, gaze changes are the dominant source of appearance variation across

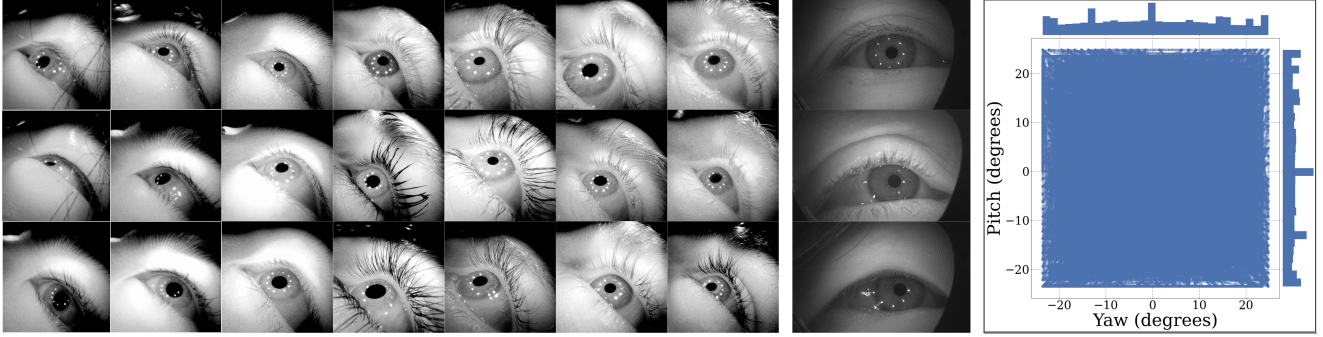


Figure 2. Sample images from our off-axis VRGaze dataset (left), example images from on-axis OpenEDS2020 dataset (center), 2D gaze angle distribution of VRGaze data (right).

frames, we train a model to transform a source frame into a target frame, conditioned on an embedding extracted from the target. The key idea is that this embedding must encode the information required to redirect the source gaze toward the target gaze. If gaze indeed explains most inter-frame differences, the learned embedding will naturally become rich in gaze-specific cues. To ensure that source–target variation is primarily gaze-related, we form training batches from pairs of frames sampled from the same eye of the same individual at different times.

#### 4.1. Separate Gaze and Appearance Encoders

To perform this generative pretext task, we extract appearance information from the source frame and gaze information from the target frame using two separate encoders.

Let  $\mathbf{x}_s$  and  $\mathbf{x}_t$  denote the source and target frames, respectively. We extract a source appearance feature map  $\mathbf{A}_s \in \mathbb{R}^{H \times W \times C_a}$  from  $\mathbf{x}_s$  using the appearance encoder  $f_{\text{app}}(\cdot)$ , and a target gaze embedding  $\mathbf{g}_t \in \mathbb{R}^{C_g}$  from  $\mathbf{x}_t$  using the gaze encoder  $f_{\text{gaze}}(\cdot)$ :

$$\mathbf{A}_s = f_{\text{app}}(\mathbf{x}_s), \quad \mathbf{g}_t = f_{\text{gaze}}(\mathbf{x}_t). \quad (1)$$

In contrast to prior work such as Cross-Encoder [30], which uses a single shared encoder for both appearance and gaze, we explicitly separate the two. We observe that gaze is an abstract, non-spatial attribute (typically described by 2 or 3 real-valued angles per frame), requiring a deep gaze encoder to match its abstraction level. In contrast, appearance is a spatial, concrete attribute, closely tied to the local image structure. Thus, the appearance encoder is designed to be shallower and preserves the 2D structure of the source frame. The architectural separation between gaze and appearance not only reflects their fundamentally different nature – but also facilitates effective disentanglement between them. This asymmetry further enables a lightweight gaze encoder and a heavier appearance encoder, with no runtime penalty, as only the gaze encoder is used during inference.

While our framework is architecture-agnostic, we target lightweight, real-time-compatible models to meet the constraints of VR and edge devices. In particular, we implement the gaze encoder using inverted bottleneck blocks from MobileNetV2 [27]. Detailed architectural descriptions of the encoders, attention modules, and decoder are provided in the supplementary material.

#### 4.2. Gaze-Conditioned Global Modulation

The appearance encoder output,  $\mathbf{A}_s$ , is refined via multi-head self-attention to capture spatial interactions, producing updated features  $\mathbf{A}'_s \in \mathbb{R}^{H \times W \times C_a}$ :

$$\mathbf{A}'_s = \text{SelfAttn}(\mathbf{A}_s) \quad (2)$$

To condition these features on the target gaze without disrupting their spatial structure, we employ a global modulation strategy. The target gaze embedding  $\mathbf{g}_t \in \mathbb{R}^{C_g}$  is linearly projected to dimension  $C_a$  and spatially replicated to form a uniform query tensor  $\mathbf{Q}_g \in \mathbb{R}^{H \times W \times C_a}$ . Using  $\mathbf{Q}_g$  as the query and  $\mathbf{A}'_s$  as the keys and values, we perform cross-attention. Because  $\mathbf{Q}_g$  is spatially uniform, this operation extracts a gaze-guided global summary of the appearance features into a uniform context tensor  $\mathbf{C} \in \mathbb{R}^{H \times W \times C_a}$ :

$$\mathbf{C} = \text{CrossAttn}(\mathbf{Q}_g, \mathbf{A}'_s, \mathbf{A}'_s) \quad (3)$$

This context is then added to the appearance features via a residual connection, yielding the fused representation  $\mathbf{F}$ :

$$\mathbf{F} = \mathbf{A}'_s + \mathbf{C} \quad (4)$$

This residual addition acts as a feature-wise global shift. It uniformly steers the latent representation toward the target gaze direction while fully preserving the structural integrity and spatial resolution of the original appearance map.

#### 4.3. Gaze-Focused Reconstruction Loss

In a standard gaze-redirection task, the model reconstructs the target image from the source using a per-pixel mean

squared error loss. This uniform weighting treats all pixels equally, forcing the model to also reconstruct regions unrelated to gaze—such as background or boundary areas. As a result, the learned gaze embedding may encode unnecessary appearance details that degrade its gaze specificity. To mitigate this issue, previous works have relied on externally defined gaze masks or handcrafted geometric priors [12, 33]. In contrast, we exploit the model’s own self-attention maps to derive adaptive spatial weights. Since in our setting most appearance variation between source and target stems from gaze changes, these attention maps naturally highlight gaze-relevant regions. We therefore use them as soft masks, emphasizing gaze-related pixels while down-weighting non-gaze regions, encouraging the model to focus reconstruction on the eye region that truly conveys gaze direction.

Since the attention weight map  $\mathbf{w}$  is computed at a lower resolution due to encoder downsampling, we first upsample  $\mathbf{w} \in \mathbb{R}^{H \times W}$  to match the spatial resolution of the target  $\mathbf{x}_t$  and reconstructed frame  $\hat{\mathbf{x}}_t$ . The *gaze-focused reconstruction loss* with a sharpening parameter  $\gamma > 0$  is defined as:

$$\mathcal{L}_{\text{focus}} = \frac{1}{\sum_i w_i^\gamma} \sum_i w_i^\gamma (x_{t,i} - \hat{x}_{t,i})^2 \quad (5)$$

where  $i$  indexes pixel locations,  $w_i$  denotes the upsampled attention weight at pixel  $i$ , and  $\gamma$  controls the sharpness of the focus.

Setting  $\gamma = 1$  recovers the standard attention-weighted loss, while  $\gamma > 1$  sharpens the attention map, increasing focus on gaze-relevant regions, and  $\gamma < 1$  softens it, distributing supervision more broadly. This self-supervised weighting scheme inherently couples attention maps with gaze representation fidelity, eliminating the need for additional regularization. Formally, for  $L_{\text{focus}} = \sum_i \tilde{w}_i (\hat{x}_i - x_i)^2$  with  $\tilde{w}_i = \frac{w_i^\gamma}{\sum_j w_j^\gamma}$  and  $\gamma > 0$ , the per-pixel gradient magnitude scales as  $\left\| \frac{\partial L_{\text{focus}}}{\partial \hat{x}_i} \right\| \propto \tilde{w}_i = \frac{w_i^\gamma}{\sum_j w_j^\gamma}$ . Increasing  $\gamma$  thus amplifies gradients in high-attention (gaze-relevant) regions and suppresses them elsewhere, providing a self-guided mechanism that focuses learning on gaze cues while reducing overfitting to peripheral variations.

#### 4.4. Gaze Calibration

After unsupervised pretraining, the model outputs latent embeddings encoding gaze direction. To derive the final gaze vector, calibration is performed differently in near-eye and remote-camera configurations. In the VR setting, where high precision is required, we apply a lightweight few-shot calibration akin to adaptation steps in self-supervised learning. A small set of labeled fixation points is used to fit a linear regressor mapping embeddings to 2D gaze angles. Because the *kappa angle*—the offset between optical and visual axes—varies across individuals, per-person calibration

is performed. Additionally, session-wise calibration before each recording compensates for minor headset slippage or repositioning, ensuring consistent gaze alignment.

For remote-camera datasets, no user-specific fitting is applied. Instead, a small MLP regressor is trained on a shared pool of 100–200 labeled samples aggregated across all subjects, following [30, 33].

## 5. Experiments

To evaluate the effectiveness of GazeShift, we conduct experiments in two settings: a *near-eye VR* setup using our newly collected VRGaze off-axis dataset and the smaller OpenEDS2020 dataset [23] (550K on-axis eye images), and a *remote-camera* setup using the Columbia [29] and MPIIGaze [35] datasets.

For the off-axis VR setting, we compare GazeShift against Cross-Encoder [30], the current leading unsupervised gaze-estimation baseline for eye-only imagery. While an earlier method by Yu and Odobez [33] also explores unsupervised gaze learning for eye images, its source code is not publicly available and its reported results are notably inferior to Cross-Encoder. Consequently, Cross-Encoder remains the only reproducible and competitive unsupervised method applicable to eye-only input, making it the most relevant baseline for this setting. (Other unsupervised approaches either require full-face or multi-view input, depend on geometric priors, or lack publicly available implementations, rendering them unsuitable for direct comparison in the off-axis VR setting.)

All training details, including hyperparameters and implementation specifics, are provided in the appendix.

### 5.1. VR Experiments

**Supervised model.** To compare GazeShift with supervised methods, we train two supervised baselines following standard gaze-estimation paradigms: an *appearance-based* binocular Siamese network that fuses left- and right-eye features to predict gaze direction, and a *feature-based* model that regresses pupil centers and glint positions, mapping the predicted features to gaze labels through linear fitting.

**Calibration protocol.** Calibration samples are extracted from fixation intervals by selecting the frame whose embedding was closest to the median within each interval. Each selected sample is paired with a 2D point-of-regard label and synchronized left and right eye images. Calibration and evaluation samples are strictly disjoint.

To evaluate gaze estimation accuracy, we map the unsupervised gaze embeddings to 2D gaze labels using ridge regression under two settings:

(1) Per-person — for each subject in the validation set,  $K \in \{17, 30, 40, 50, 60\}$  fixation points are randomly sampled for calibration, and the remaining fixation points are

Table 3. Performance on VRGaze.

Supervision	Method	Calibration Type	Avg. Error [°]
Supervised	Appearance Based	Per-person	<b>1.54</b>
	Feature Based		3.2
Unsupervised	VAE		5.30
	Cross-Encoder		2.15
	GazeShift	<b>1.84</b>	
	Cross-Encoder	Person-agnostic	2.83
	GazeShift	Person-agnostic (K=100)	<b>2.73</b>
	Cross-Encoder	Person-agnostic (K=200)	2.26
GazeShift	Person-agnostic (K=200)	<b>2.13</b>	

Table 4. Performance on OpenEDS2020.

Model	Calibration Type	Avg. Error [°]
Cross-Encoder	Per-person	3.69
GazeShift	Per-person	<b>3.43</b>
Cross-Encoder	Person-agnostic	5.20
GazeShift	Person-agnostic	<b>4.20</b>

Table 5. GazeShift ablation study on VRGaze.

#	Separate Encoders	Attention-Based Redirection	Gaze-Focused Loss	Avg. Error [°]
1	×	×	×	2.15
2	✓	×	×	2.10
3	✓	✓	×	2.07
4	✓	✓	✓	<b>1.84</b>

used exclusively for evaluation. Results are averaged over 10 random splits across  $K$  values and subjects.

(2) Person-agnostic — a single regressor is trained using  $K \in \{100, 200\}$  labeled fixation points pooled across validation subjects, with the remaining samples used for evaluation. Results are averaged over 10 runs.

**VRGaze results.** As shown in Table 3, GazeShift consistently outperforms prior unsupervised baselines across all calibration settings, reaching a mean error of **1.84°** under per-person calibration and maintaining competitive accuracy under person-agnostic evaluation. These results confirm that the attention-based redirection and gaze-aware loss are particularly effective for handling the geometric distortions and illumination variability characteristic of off-axis headset-mounted sensors.

**OpenEDS2020 results.** To evaluate GazeShift under on-axis conditions, we trained it on the OpenEDS2020 dataset using Cross-Encoder as the baseline. As summarized in Table 4, GazeShift consistently outperforms Cross-

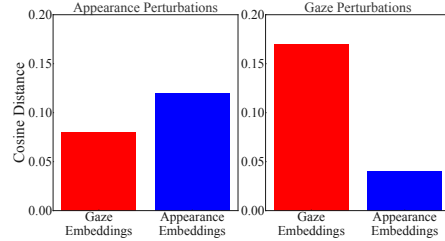


Figure 3. Disentanglement analysis of learned embeddings. Left: Appearance Perturbations — same gaze, varying appearance. Right: Gaze Perturbations — same appearance, varying gaze. Gaze embeddings vary primarily with gaze direction, while appearance embeddings remain stable, demonstrating effective disentanglement.

Encoder, achieving lower errors in both per-person and person-agnostic ( $K=100$ ) calibration protocols. These results demonstrate that the proposed attention-based representation and gaze-aware loss transfer effectively across different camera geometries and VR headset designs, highlighting the model’s robustness to geometric and photometric variations in real-world conditions.

**Cross-Dataset generalization from on-axis to off-axis data.** To assess the importance of off-axis data, we evaluate whether a model trained on existing on-axis datasets can generalize to off-axis conditions. As illustrated in Figure 2, the appearance differences between on-axis and off-axis imagery are substantial, with strong perspective and illumination shifts. We train GazeShift on the on-axis OpenEDS2020 dataset and test it on the VRGaze validation set, obtaining a mean error of  $5.2^\circ$  under the per-person calibration protocol—compared to  $1.84^\circ$  when trained directly on VRGaze. This large gap highlights that models trained on on-axis data fail to capture the geometric distortions characteristic of off-axis near-eye cameras, underscoring the necessity of dedicated datasets such as VRGaze for accurate and robust VR gaze estimation.

**Validating gaze–appearance disentanglement** To examine GazeShift’s assumption that inter-frame appearance variation primarily reflects gaze shifts, we analyze embedding sensitivity to both gaze and appearance perturbations (Figure 3). For appearance perturbations, we augment a single eye image with 100 illumination and contrast variations, keeping gaze fixed. For gaze perturbations we sampled 80 images of the same eye with distinct gaze directions but similar lighting. In both experiments, we compute the average cosine distances across all gaze embeddings and all appearance embeddings. Under appearance perturbations, gaze embeddings remained stable (0.08 average cosine distance) while appearance embeddings varied moderately (0.12). Under gaze perturbations, gaze embeddings changed substantially (0.17) whereas appearance embeddings remained nearly constant (0.04). This analysis

Table 6. Average error under different  $\gamma$  settings.

$\gamma$	0.5	1.0	2.0	4.0
Avg. Error [ $^{\circ}$ ]	2.03	<b>1.84</b>	2.19	2.41

show that GazeShift disentangles gaze from appearance.

**Attention visualization.** Figure 4 presents example source appearance images alongside their corresponding self-attention maps. The model learns to focus on regions that exhibit the greatest appearance differences between the source and target images—primarily the gaze-relevant areas around the iris.

**Model efficiency and on-device runtime.** Our lightweight gaze encoder contains 342K parameters and requires 55 MFLOPs. To assess deployment feasibility, we implemented GazeShift gaze encoder on our custom VR headset equipped with an Exynos 2200 chipset. Running on the Xclipse 920 mobile GPU, average runtime for both eyes was measured at 5 ms, confirming GazeShift’s suitability for real-time, on-device gaze applications.

**Ablations studies.** We systematically evaluate each component of the GazeShift framework on the VRGaze dataset, with results summarized in Table 5. The baseline configuration uses a single shared encoder for both gaze and appearance, with concatenated features and a standard  $\ell_2$  reconstruction loss, yielding an average error of  $2.15^{\circ}$ . Splitting the encoder into distinct gaze and appearance branches reduces the error to  $2.10^{\circ}$ , confirming the benefit of disentangled representations. Incorporating cross-attention further lowers the error to  $2.07^{\circ}$ , as it enables direct conditioning of appearance features on gaze information. Crucially, this attention mechanism also makes possible the gaze-focused reconstruction loss, which leverages attention maps to weight supervision on gaze-relevant regions—yielding the largest improvement, down to  $1.84^{\circ}$ .

**Gaze-focused loss sensitivity.** We experimented with various  $\gamma$  values. The results are presented in Table 6. When  $\gamma = 1$ , the weighting follows the model’s raw attention, giving a balanced emphasis on gaze-relevant regions. For  $\gamma > 1$ , supervision becomes too narrow: the loss overshoots and neglects surrounding contextual cues (eyelid edges, glints, etc.), which actually hurts the gaze embedding stability. For  $\gamma < 1$ , it’s too diffused, blurring gaze vs. appearance signals.

## 5.2. Remote Camera Experiments

As demonstrated, GazeShift performs well on our VR off-axis dataset. We next establish its ability to generalize to the remote-camera setting.

The core idea behind GazeShift is that the pretext task of gaze redirection can produce meaningful gaze embeddings when the primary variation between paired images

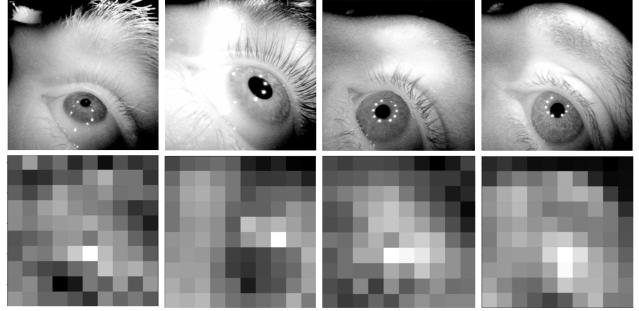


Figure 4. **Appearance source frames and their associated self-attention maps.** The model learns to focus on regions that exhibit the greatest differences between the source and target images—primarily the gaze-relevant areas around the iris.

is driven by changes in gaze direction. In remote camera settings, however, this assumption is less reliable due to increased variation from inconsistent eye cropping, illumination changes, and other in-the-wild factors.

To evaluate GazeShift in this regime, we aim to maximize gaze-induced variation while minimizing irrelevant appearance differences. We use two publicly available datasets representing different levels of environmental control.

**Columbia Gaze** consists of 6,000 face images from 56 subjects captured in a controlled laboratory environment. Each image is labeled with one of five discrete head poses and 21 gaze directions. To ensure that pairwise variation is gaze-specific, during training, we sample redirection pairs from within the same head pose category.

**MPIIGaze** contains 213,659 images of 15 subjects recorded in everyday conditions while seated in front of a laptop screen. Since the dataset was collected in uncontrolled environments, it exhibits significant variation in non-gaze factors such as lighting and background. To mitigate this, we sample training pairs from the same video using a short temporal window, promoting appearance similarity outside of gaze.

The input images have a resolution of  $64 \times 32$ , in contrast to the  $400 \times 400$  resolution of VRGaze. Consequently, we construct the gaze encoder with a different configuration of MobileNetV2 blocks. For appearance encoding, we employ a ResNet-18, consistent with the Cross-Encoder paper [30].

In our first experiment, we train the model on the Columbia Gaze dataset in an unsupervised manner and evaluate its performance on MPIIGaze. Following the evaluation protocol used by Cross-Encoder, we adopt a leave-one-subject-out cross-validation scheme. Specifically, for each test subject, we train a shallow MLP regressor in a 100-shot supervised setting: 100 embeddings are randomly sampled from the remaining subjects and used as training data. This procedure is repeated for all 15 subjects in MPIIGaze, and

Table 7. Calibration results on MPIIGaze using embeddings trained on Columbia Gaze.

Supervision	Method	Avg. Error [°]	Params	FLOPS
Supervised	Resnet-18	8.35	11M	75M
Unsupervised	Cross-Encoder	8.32	11M	75M
	GazeShift (MobileNetV2)	8.00	<b>1M</b>	<b>2M</b>
	GazeShift (ResNet-18)	<b>7.56</b>	11M	75M

we report the average angular error across all folds.

We compare our method to Cross-Encoder and a supervised baseline using ResNet-18 trained on three public datasets (Columbia, UTMultiview, and XGaze [36]) as described in [30]. The results are shown in Table 7. To comprehensively evaluate our architecture, we conducted two experiments with GazeShift: one equipped with our lightweight MobileNetV2-based gaze encoder and another utilizing a ResNet-18 gaze encoder. The lightweight GazeShift achieves an error of  $8.00^\circ$ , outperforming Cross-Encoder ( $8.32^\circ$ ) and the supervised baseline ( $8.35^\circ$ ) while operating with 35x fewer FLOPS and 10x fewer parameters than Cross-Encoder. Furthermore, when scaling GazeShift gaze encoder to use ResNet-18, our accuracy improves to  $7.56^\circ$ , demonstrating superior representation learning while utilizing the exact same compute budget as Cross-Encoder.

In the second experiment, we follow the Cross-Encoder protocol and fine-tune the model – initially trained on Columbia Gaze – on MPIIGaze using unsupervised learning. For each fold, we train the model on 14 subjects and evaluate on the held-out subject using the 100-shot protocol, where a supervised MLP is trained on 100 embeddings sampled from the training subjects. Table 8 summarizes the results. The results of all models except GazeShift are taken from [30]. GazeShift achieves the best performance while using 10x fewer parameters.

### 5.2.1. Qualitative Results on Gaze Representation

To visually evaluate the continuity of the latent space and gaze-appearance disentanglement, we perform a latent space interpolation experiment (Figure S6). By linearly interpolating between two target gaze vectors while conditioning on fixed appearance embeddings, the generated sequences produce a smooth, continuous eye movement. Crucially, the model preserves the unique features of the source identity without allowing appearance characteristics from the target gaze image to leak into the reconstruction. This confirms that GazeShift learns a structured, disentangled manifold.

## 6. Limitations

GazeShift assumes that most inter-frame appearance variation reflects gaze changes. In the VR domain, this assumption largely holds, as illumination and camera placement

Table 8. Unsupervised fine-tuning results on MPIIGaze.

Model	Avg. Error [°]	Params
ResNet-18 (ImageNet)	10.60	11M
Auto-encoder	9.50	11M
Auto-encoder (EFC)	9.20	11M
SimCLR	10.00	25M
BYOL	11.10	25M
Cross-Encoder	7.20	11M
GazeShift (MobileNetV2)	<b>7.15</b>	<b>1M</b>

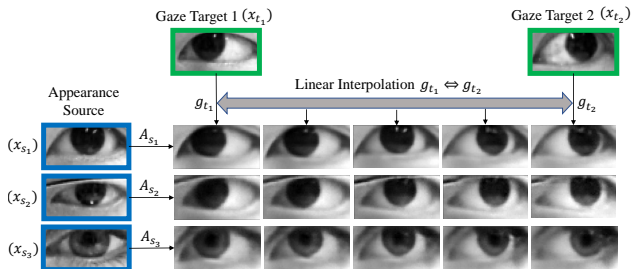


Figure 5. **Latent space interpolation and gaze redirection.** We interpolate between two target gaze embeddings ( $g_{t_1} \rightarrow g_{t_2}$ , top green boxes) while keeping the appearance embeddings ( $A_{s_1}, A_{s_2}, A_{s_3}$ , left blue boxes) fixed for each row. The smooth eye movement between the gaze targets, combined with the preservation of the source images’ unique appearance, visually confirms effective disentanglement and a continuous latent manifold.

are tightly controlled. Appearance variations that do not correspond to gaze—such as brief blinks, eyelid motion, or pupil dilation—occur infrequently and thus have minimal effect on model performance. However, in augmented reality (AR) or mixed-reality settings, where lighting conditions and reflections are less constrained, the impact of such non-gaze appearance variations remains an open question for future investigation.

## 7. Conclusion

Despite the growing XR market, progress in VR gaze estimation remains hindered by the lack of suitable datasets and methods. We address both challenges by introducing VRGaze, a large-scale off-axis VR dataset, and GazeShift, an unsupervised method that eliminates the need for accurate labels while achieving sub- $2^\circ$  error—making it suitable for practical deployment. Implemented directly on a VR device, our gaze encoder runs in **5 ms** on the device GPU, demonstrating its value for real-time inference on edge hardware. Beyond gaze estimation, GazeShift provides a general framework for unsupervised representation learning from paired transformations. Its attention-guided redirection and self-supervised loss formulation can extend to other domains where appearance changes encode structured variation, such as facial motion, head-pose, or viewpoint-conditioned representations.

## References

- [1] Yiwei Bao, Yihua Cheng, Yunfei Liu, and Feng Lu. Adaptive feature fusion network for gaze tracking in mobile tablets. In *2020 25th International Conference on Pattern Recognition (ICPR)*, pages 9936–9943. IEEE, 2021. 2
- [2] Kathrin Berkner-Cieslicki, Ricardo J. Motta, Se Hoon Lim, Minwoong Kim, Kenichi Saito, Branko Petljanski, Jason C. Sauer, and Yoshikazu Shinohara. Eye tracking system, 2020. US Patent 10,877,556. Assignee: Apple Inc. 3
- [3] Mathilde Caron, Hugo Touvron, Ishan Misra, Hervé Jégou, Julien Mairal, Piotr Bojanowski, and Armand Joulin. Emerging properties in self-supervised vision transformers. In *Proceedings of the IEEE/CVF International Conference on Computer Vision (ICCV)*, pages 9650–9660, 2021. 1
- [4] H. Cecotti, Y. K. Meena, B. Bhushan, A. Dutta, and G. Prasad. A multiscript gaze-based assistive virtual keyboard. In *2019 41st Annual International Conference of the IEEE Engineering in Medicine and Biology Society (EMBC)*, pages 1306–1309, 2019. 1
- [5] Yihua Cheng, Xucong Zhang, Feng Lu, and Yoichi Sato. Gaze estimation by exploring two-eye asymmetry. *IEEE Transactions on Image Processing*, 29:5259–5272, 2020. 2
- [6] Andrew T. Duchowski. *Eye Tracking Methodology: Theory and Practice*. Springer, 2017. 1
- [7] Wolfgang Fuhl, Gjergji Kasneci, and Enkelejda Kasneci. Teyed: Over 20 million real-world eye images with pupil, eyelid, and iris 2d and 3d segmentations, 2d and 3d landmarks, 3d eyeball, gaze vector, and eye movement types. In *IEEE International Symposium on Mixed and Augmented Reality (ISMAR)*, pages 367–375, 2021. 3
- [8] John Gideon, Shan Su, and Simon Stent. Unsupervised multi-view gaze representation learning. In *Proceedings of the IEEE/CVF Conference on Computer Vision and Pattern Recognition Workshops (CVPRW)*, pages 4997–5005, 2022. 3
- [9] Jean-Bastien Grill, Florian Strub, Florent Altché, Corentin Tallec, Pierre Richemond, Elena Buchatskaya, Carl Doersch, Bernardo Avila Pires, Zhaohan Guo, Mohammad Gheshlaghi Azar, Bilal Piot, Koray Kavukcuoglu, Remi Munos, and Michal Valko. Bootstrap your own latent: A new approach to self-supervised learning. In *Advances in Neural Information Processing Systems*, pages 21271–21284. Curran Associates, Inc., 2020. 1
- [10] Kaiming He, Haoqi Fan, Yuxin Wu, Saining Xie, and Ross Girshick. Momentum contrast for unsupervised visual representation learning. In *Proceedings of the IEEE/CVF Conference on Computer Vision and Pattern Recognition (CVPR)*, pages 9729–9738, 2020. 1
- [11] HTC Corporation. Htc vive pro eye – technical specifications. <https://developer.vive.com/resources/hardware-guides/vive-pro-eye-specs-user-guide/>. Accessed: 2026-02-24. 3
- [12] Yangzhou Jiang, Yinxin Lin, Yaoming Wang, Teng Li, Bilian Ke, and Bingbing Ni. Learning unsupervised gaze representation via eye mask driven information bottleneck. *arXiv preprint arXiv:2407.00315*, 2024. 5
- [13] Swati Jindal and Roberto Manduchi. Contrastive representation learning for gaze estimation. In *Gaze Meets Machine Learning Workshop*, pages 37–49. PMLR, 2023. 3
- [14] Harsimran Kaur, Swati Jindal, and Roberto Manduchi. Rethinking model-based gaze estimation. *Proceedings of the ACM on Computer Graphics and Interactive Techniques*, 5(2):1–17, 2022. 2
- [15] JooHwan Kim, Michael Stengel, Alexander Majercik, Shalini De Mello, David Dunn, Samuli Laine, Morgan McGuire, and David Luebke. Nvgaze: An anatomically-informed dataset for low-latency, near-eye gaze estimation. In *Proceedings of the 2019 CHI Conference on Human Factors in Computing Systems*, pages 1–12, 2019. 2, 3
- [16] Kuno Kurzhals, Fabian Göbel, Katrin Angerbauer, Michael Sedlmair, and Martin Raubal. A view on the viewer: Gaze-adaptive captions for videos. In *Proceedings of the 2020 CHI Conference on Human Factors in Computing Systems*, pages 1–12, 2020. 3
- [17] Zequan Lian, Tao Xu, Zhen Yuan, Junhua Li, Nitish Thakor, and Hongtao Wang. Driving fatigue detection based on hybrid electroencephalography and eye tracking. *IEEE Journal of Biomedical and Health Informatics*, 2024. 1
- [18] Poika Majaranta and Andreas Bulling. Eye tracking and eye-based human–computer interaction. In *Advances in Physiological Computing*, pages 39–65. Springer, 2014. 1
- [19] Katerina Mania, Ann McNamara, and Andreas Polychronakis. Gaze-aware displays and interaction. In *ACM SIGGRAPH 2021 Courses*, pages 1–67. 2021. 1
- [20] Meta Platforms, Inc. Building eye tracking on meta quest pro responsibly. <https://securecdn.oculus.com/sr/meta-quest-pro-eye-tracking-white-paper>. Accessed: 2026-02-24. 3
- [21] Francisco Muñoz-Leiva, María Eugenia Rodríguez-López, and Bárbara García-Martí. Discovering prominent themes of the application of eye tracking technology in marketing research. *Cuadernos de Gestión*, 22(1):97–113, 2022. 1
- [22] Jaekwang Oh, Youngkeun Lee, Jisang Yoo, and Soonchul Kwon. Improved feature-based gaze estimation using self-attention module and synthetic eye images. *Sensors*, 22(11):4026, 2022. 2
- [23] Cristina Palmero, Abhishek Sharma, Karsten Behrendt, Kapil Krishnakumar, Oleg V. Komogortsev, and Sachin S. Talathi. Openeds2020: Open eyes dataset. *arXiv preprint arXiv:2005.03876*, 2020. 3, 5
- [24] Seonwook Park, Adrian Spurr, and Otmar Hilliges. Deep pictorial gaze estimation. In *Proceedings of the European Conference on Computer Vision (ECCV)*, pages 721–738, 2018. 2
- [25] Anjul Patney, Marco Salvi, Jae-Pil Kim, Anton Kaplanyan, Chris Wyman, Nate Benty, Aaron Lefohn, and David Luebke. Towards foveated rendering for gaze-tracked virtual reality. In *ACM SIGGRAPH 2016 Emerging Technologies*. ACM, 2016. 1
- [26] Ken Pfeuffer, Michael Geiger, Daniel Buschek, and Florian Alt. Gaze+pinch interaction in virtual reality. In *Proceedings of the 30th Annual ACM Symposium on User Interface Software and Technology*, pages 547–559. ACM, 2017. 1

- [27] Mark Sandler, Andrew Howard, Menglong Zhu, Andrey Zhmoginov, and Liang-Chieh Chen. Mobilenetv2: Inverted residuals and linear bottlenecks. In *Proceedings of the IEEE Conference on Computer Vision and Pattern Recognition*, pages 4510–4520, 2018. [4](#)
- [28] Ludwig Sidenmark, Dominic Potts, Bill Baptsch, and Hans Gellersen. Radi-eye: Hands-free radial interfaces for 3d interaction using gaze-activated head-crossing. In *Proceedings of the 2021 CHI Conference on Human Factors in Computing Systems*, pages 1–11, 2021. [1](#)
- [29] Brian A. Smith, Qi Yin, Steven K. Feiner, and Shree K. Nayar. Gaze locking: Passive eye contact detection for human-object interaction. In *Proceedings of the 26th Annual ACM Symposium on User Interface Software and Technology*, pages 271–280, 2013. [5](#)
- [30] Yunjia Sun, Jiabei Zeng, Shiguang Shan, and Xilin Chen. Cross-encoder for unsupervised gaze representation learning. In *ICCV*, pages 3702–3711, 2021. [1](#), [2](#), [4](#), [5](#), [7](#), [8](#)
- [31] Yaoming Wang, Jin Li, Wenrui Dai, Bowen Shi, Xiaopeng Zhang, Chenglin Li, and Hongkai Xiong. Bootstrap autoencoders with contrastive paradigm for self-supervised gaze estimation. In *Proceedings of the 41st International Conference on Machine Learning*, pages 50794–50806. PMLR, 2024. [3](#)
- [32] Xiaobao Wei, Peng Chen, Guangyu Li, Ming Lu, Hui Chen, and Feng Tian. Gazegaussian: High-fidelity gaze redirection with 3d gaussian splatting. In *ICCV*, pages 13293–13303, 2025. [1](#), [3](#)
- [33] Yu Yu and Jean-Marc Odobez. Unsupervised representation learning for gaze estimation. In *CVPR*, pages 7314–7324, 2020. [1](#), [2](#), [3](#), [5](#)
- [34] Xucong Zhang, Yusuke Sugano, Mario Fritz, and Andreas Bulling. It’s written all over your face: Full-face appearance-based gaze estimation. In *Proceedings of the IEEE Conference on Computer Vision and Pattern Recognition Workshops*, pages 51–60, 2017. [2](#)
- [35] Xucong Zhang, Yusuke Sugano, Mario Fritz, and Andreas Bulling. Mpiigaze: Real-world dataset and deep appearance-based gaze estimation. *IEEE Transactions on Pattern Analysis and Machine Intelligence*, 41(1):162–175, 2019. [1](#), [5](#)
- [36] Xucong Zhang, Seonwook Park, Thabo Beeler, Derek Bradley, Siyu Tang, and Otmar Hilliges. Eth-xgaze: A large scale dataset for gaze estimation under extreme head pose and gaze variation. In *ECCV*, pages 365–381. Springer, 2020. [8](#)
- [37] Xiaolong Zhou, Haibin Cai, Youfu Li, and Honghai Liu. Two-eye model-based gaze estimation from a kinect sensor. In *2017 IEEE International Conference on Robotics and Automation (ICRA)*, pages 1646–1653. IEEE, 2017. [2](#)

# Supplementary Material

## A. GazeShift: Implementation Details and Qualitative Results

As VRGaze and remote-camera datasets such as Columbia and MPIIGaze differ in input resolution, we adopt architecture variations tailored to each. All experiments were conducted on a single NVIDIA RTX A5000 GPU. Our GazeShift code and VRGaze dataset are available here: <https://github.com/gazeshift3/gazeshift>

### A.1. VR Experimental Details

The VRGaze input resolution is  $1 \times 400 \times 400$ . To support real-time inference on a VR headset, the gaze encoder is designed to be lightweight: it consists of 6 stride-2 MobileNetV2 blocks, each repeated twice and configured with a width multiplier of 2. A final linear layer projects the output to a gaze embedding of dimension  $C_d$ .

The appearance encoder consists of a stride-2 convolution, followed by four MobileNetV2 blocks, each repeated six times, and a final stride-1 convolutional layer, producing a feature map of size  $10 \times 10 \times C_a$ . The attention module employs a single-layer, single-head attention mechanism. The decoder is composed of transposed convolutional blocks, each followed by batch normalization and a  $\tanh$  activation.

The model is trained for 20 epochs with a batch size of 30 using the AdamW optimizer, a learning rate of 0.0001, and a weight decay of 0.05.

#### A.1.1. VAE baseline details

The VAE baseline (Table 3 in the paper) employs an architecture analogous to GazeShift, utilizing a MobileNetV2-based image encoder and a matching decoder. It is trained strictly via a standard image reconstruction objective on the input frames.

#### A.1.2. Supervised Appearance-based Model

To contextualize the performance of GazeShift, we train a supervised binocular model using the same lightweight gaze encoder architecture. Training samples are selected from intervals where the gaze target remains stationary for three seconds, ensuring higher label reliability compared to periods of target motion. We adopt a simple Siamese configuration: synchronized left and right eye images serve as input, with the right-eye images horizontally flipped to reduce appearance asymmetry and improve representation learn-

ing. The resulting embeddings are concatenated and passed through a regression head to predict 3D gaze direction.

**Calibration aware loss.** In conventional gaze regression models, the training loss is computed directly on raw outputs, ignoring the calibration step typically performed at inference. We propose integrating calibration directly into training by applying the loss to calibrated outputs. Specifically, we implement a linear calibration module in PyTorch that fits polynomial features to the batch-level predictions. This module is treated as a differentiable layer, allowing the model to optimize for post-calibration accuracy and better align with real-world inference behavior. Calibration aware loss reduced the average error from  $1.64^\circ$  to  $1.54^\circ$ . Fig. S1 depicts our supervised model architecture.

### A.2. Remote Camera Experimental Details

In the remote camera setting, the input resolution of each eye crop is  $64 \times 32$ . The gaze encoder consists of 3 MobileNetV2 blocks, while the appearance encoder follows a ResNet-18 backbone, similar to the configuration used in Cross-Encoder. The attention module uses 2 layers with 2 heads, and the decoder is implemented using a DenseNet architecture.

Unlike the near-eye setting, both eye crops in the remote setup are extracted from the same image, resulting in similar appearance characteristics. We leverage this symmetry by generating source–target pairs not only from different time steps of the same eye, but also by using synchronized left/right eye pairs – where one image is horizontally flipped to simulate a plausible gaze shift.

## B. VRGaze Dataset: Additional Characteristics and Collection Information

**Target motion pattern.** Figure S2 illustrates the distribution of gaze targets for a single person over multiple sessions. Linear segments are formed by a slowly moving ball to induce smooth pursuit eye movements. The nodes at the ends of the segments are stationary points intended to elicit eye fixations. Thus, each session consists of a ball moving slowly along straight trajectories, followed by an abrupt stop lasting three seconds. During each stop, the ball gradually changes in size to enhance the fixation.

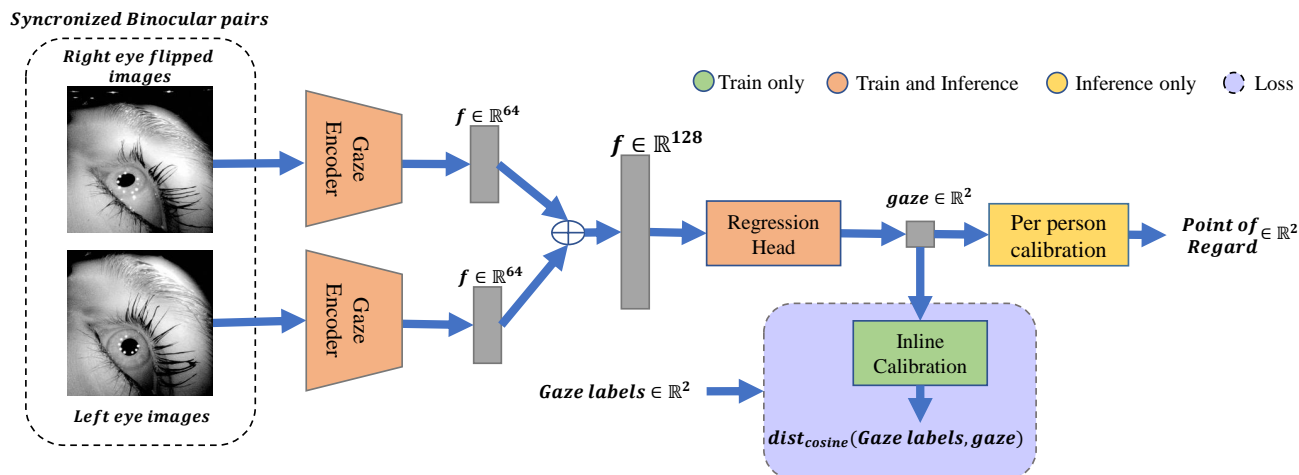


Figure S1. Supervised model architecture.

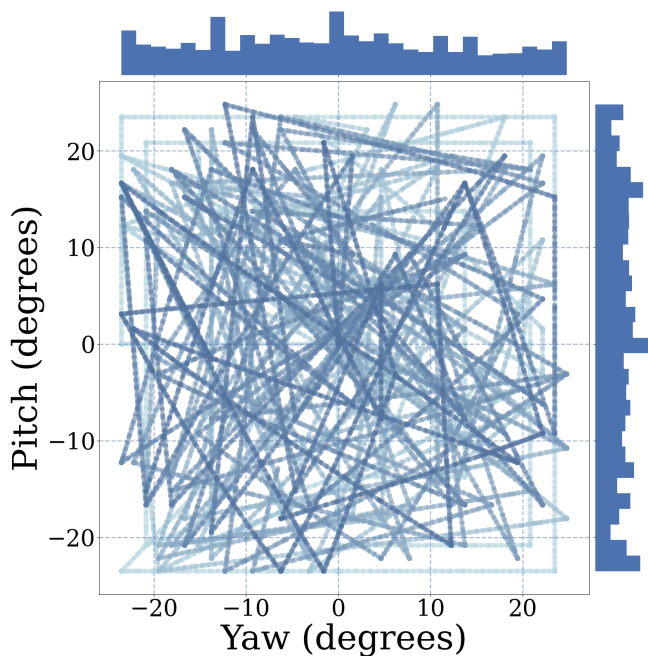


Figure S2. Single person data visualization.

**Gaze direction diversity.** To illustrate the range of gaze directions captured, we present in Fig. S3 nine example eye images corresponding to different target positions, including center, corners, and cardinal directions (left, right, up, down). This visualization demonstrates how eye appearance varies with gaze angle, providing qualitative insight into VRGaze dataset.

**Pupil dilation diversity.** To ensure the robustness of gaze tracking under varying lighting conditions and physiological responses, we collected eye images exhibiting a wide range of pupil sizes. This was achieved by varying the background brightness during data collection sessions in VR, prompting natural pupil dilation and constriction. Fig. S4 illustrates examples of eye images with different pupil diameters, highlighting the captured diversity. Such variation is essential for training models that generalize well across

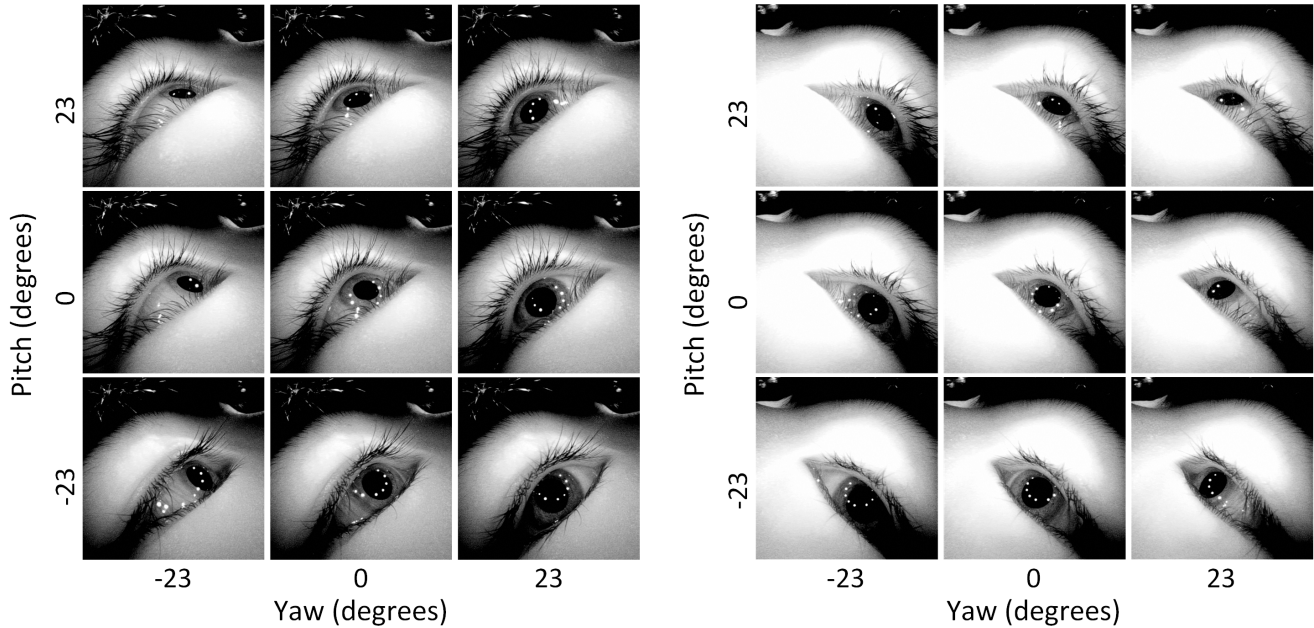


Figure S3. Gaze direction visualization.

users and lighting environments.

**Pupil Center and Glint Annotations** IR LED reflections (glints) are typically visible in VR cameras and may also be used for gaze estimation. To promote future research, we also release coordinates of pupil center and glints for each image in VRGaze. To obtain the pupil and glints coordinates for the entire dataset, we manually annotated 32k images which were used to train a feature detection model to annotate the rest. We trained the model on 28k images and evaluated it on a validation set of 4k images, achieving mean accuracies of 0.54 and 0.96 pixels for pupil and glint detection, respectively. Fig. S5 illustrates annotated and predicted features. The pupil center is illustrated with a blue circle, visible glints with green circles, and undetected glints with red circles.

### C. VR Device specifications

The VRGaze dataset was collected using a custom virtual reality headset prototype equipped with a dedicated off-axis eye tracking system. To validate the real-time capabilities of the GazeShift architecture, all on-device processing and inference benchmarking were executed on a Samsung Exynos 2200 System-on-Chip featuring an Xclipse 920 mobile GPU. This setup accurately reflects the thermal and computational constraints of modern standalone extended reality devices. The camera operates at 30 frames per second with a spatial resolution of 400x400 pixels, and the device provides a 90° horizontal field of view. Active illumi-

nation is supplied by an array of 10 near-infrared LEDs per eye. The camera sensor is mounted at a steep oblique angle below the eye (Figure S8) to mimic the restrictive internal layouts required by modern, slim VR form factors. Finally, strict temporal synchronization between the display rendering the visual stimulus and the camera's capture trigger ensures precise 2D Point of Regard ground truth labels across all 2.1 million recorded frames.



Figure S4. Pupils dilation illustration.

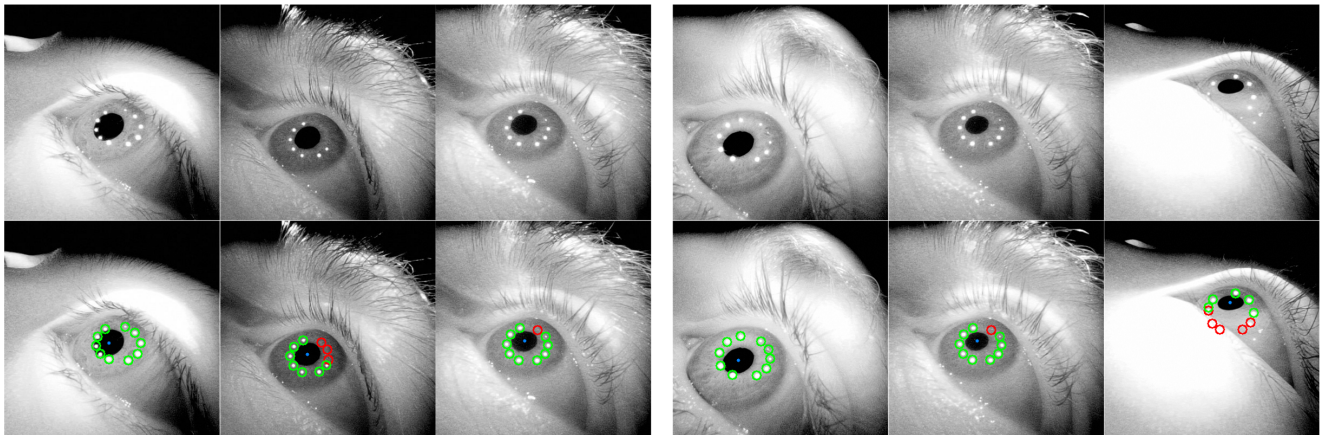


Figure S5. Pupil center and glints from manual annotations (left) and model predictions (right).

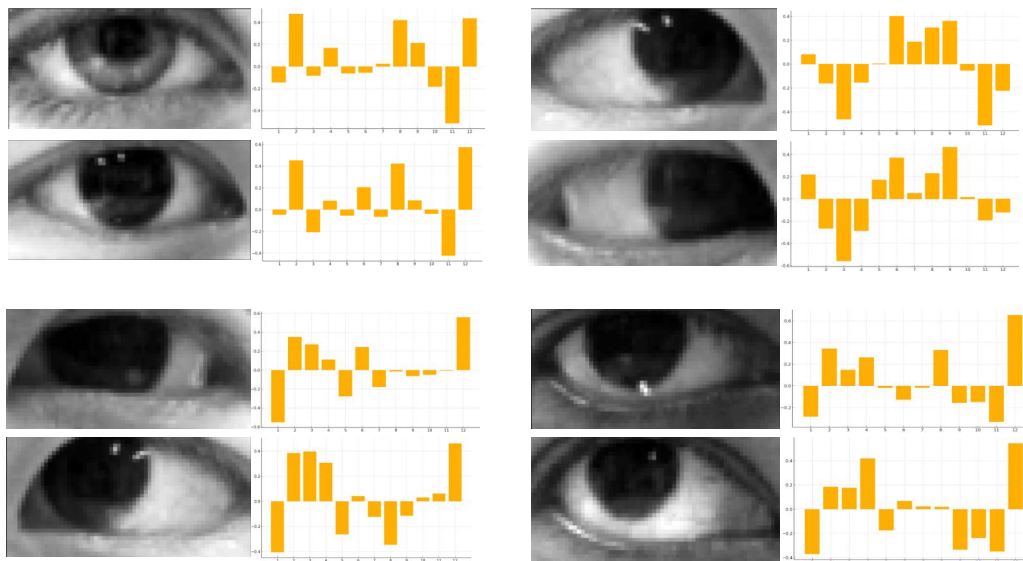


Figure S6. Gaze embeddings across directions. Each quadrant shows two eye images with similar gaze directions, along with their corresponding 12D gaze embeddings. Within a quadrant, the embeddings align closely, while embeddings across quadrants differ, reflecting distinct gaze directions. Notably, in the top-left quadrant, the gaze embeddings remain similar despite clear differences in eye appearance.

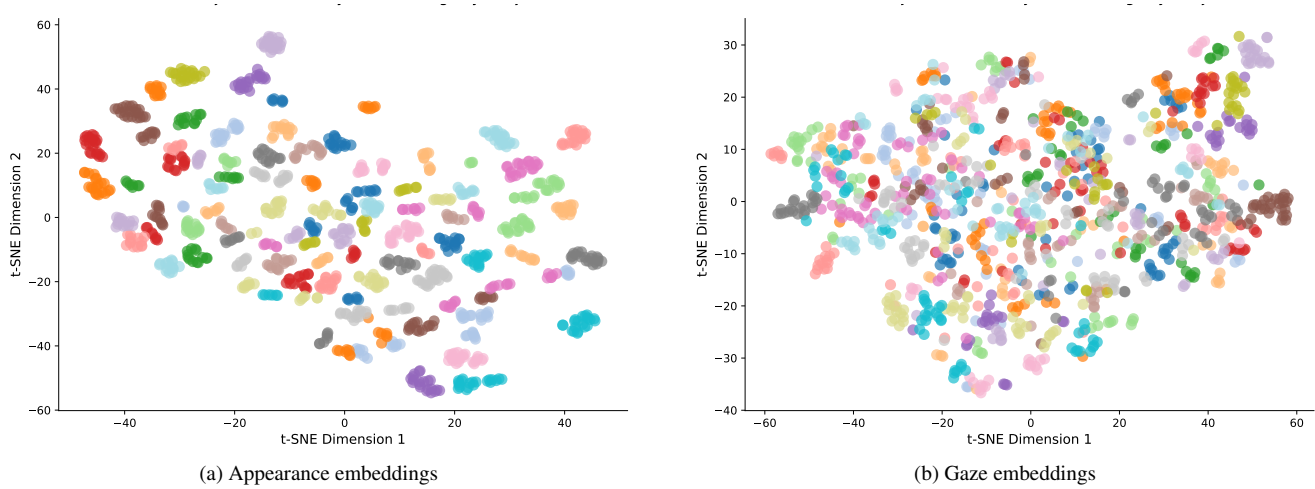


Figure S7. **Latent space visualization.** A t-SNE projection of the representations extracted by GazeShift. Each point corresponds to an eye image from the Columbia Gaze dataset and is colored according to the subject's identity, illustrating the clustering of appearance features.

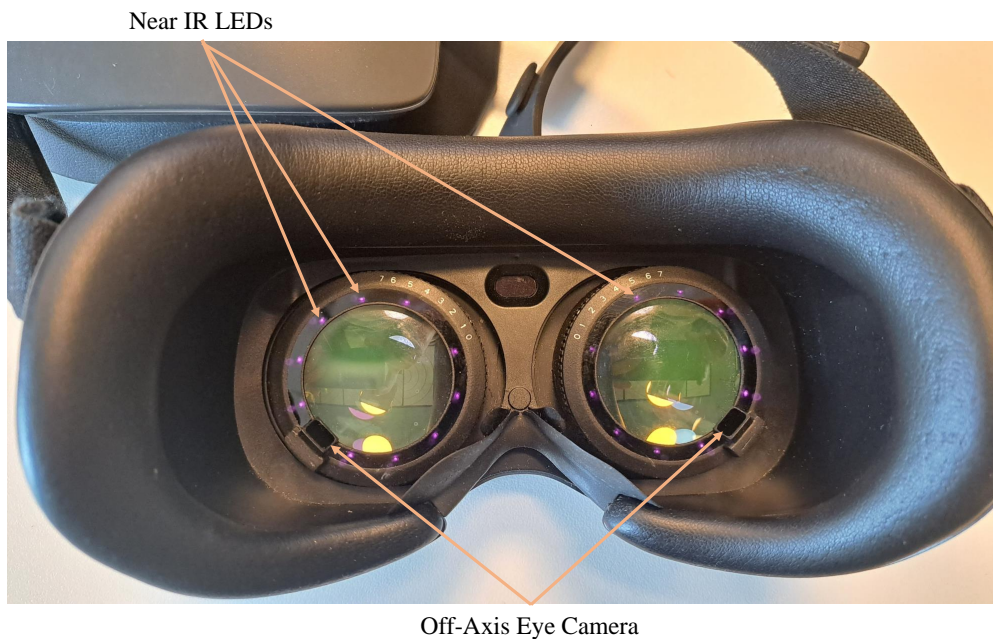


Figure S8. **VRGaze hardware setup.** The internal view of the custom virtual reality headset used for data collection. The ring of 850 nm near-infrared LEDs (visible as purple lights) provides active illumination for robust corneal glint formation, while the restrictive form factor necessitates the off-axis camera placement.